Power Engineering and Engineering Thermophysics
https://www.acadlore.com/journals/PEET

Numerical Examination of Heat Transfer and Entropy Generation in Confined-Slot Jet Impingement Featuring Wing Ribs

Mohammed Abed Ahmed[1*], Saad M. Hatem[1], Ibrahim K. Alabdaly[2]

[1] Department of Mechanical Engineering, College of Engineering, University of Anbar, 31001 Anbar, Iraq
[2] Department of Chemical and Petrochemical, College of Engineering, University of Anbar, 31001 Anbar, Iraq

[*] Correspondence: Mohammed Abed Ahmed (mohammed.abed@uoanbar.edu.iq)

Received: 08-20-2023 **Revised:** 09-19-2023 **Accepted:** 09-25-2023

Citation: M. A. Ahmed, S. M. Hatem, and I. K. Alabdaly, "Numerical examination of heat transfer and entropy generation in confined-slot jet impingement featuring wing ribs," *Power Eng. Eng. Thermophys.*, vol. 2, no. 3, pp. 173–187, 2023. https://doi.org/10.56578/peet020305.

Abstract: In this study, a numerical investigation into heat transfer and entropy generation characteristics using confined-slot jet impingement was conducted. Comparisons were drawn between the heat transfer and entropy generation attributes of two wing ribs positioned on the heated impinging target surface and those of a rib-less surface. The influences of variations in the spacing between the stagnation point and the rib (B) of (10-30 mm), ranging from 10 to 30 mm, rib heights (A) between 0.5 to 2 mm, and a Reynolds number of the jet (Re) between 3000 to 8000 on fluid flow, heat transfer, and entropy generation were elucidated. Employing the Finite Volume Method (FVM) managed the continuity, momentum, and energy equations in adherence to the principles of the SIMPLE methodology. Results revealed that the Nusselt number $(\overline{Nu})$, pressure drop, and total entropy $\left(\bar{S}_{\text{total}}\right)$ escalated in accordance with Re and A. Conversely, they diminished with reduced spacing from the stagnation point to B. Notably, a superior heat transfer rate was observed when employing a target plate integrated with wing ribs in contrast to a rib-less configuration. Performance Evaluation Criteria (PEC) values were noted to augment with rib height increment. It is demonstrated that the PEC increases as A increases. Also, the lower value of PEC equals 1.044 at A of 2 mm, B of 10 mm, and Re of 8000, while the higher value of the PEC equals 1.68 at A of 2 mm, B of 10 mm, and Re of 3000. The findings suggest that slot-Jet impingement complemented by wing ribs plays a pivotal role in enhancing the cooling efficiency of electronic devices.

Keywords: Impinging orifice-jet; Wing ribs; Finite Volume Method; Heat transfer characteristic; Entropy generation; Turbulent flow; Numerical investigation

1 Introduction

The technique of impinging jets has emerged as a prevalent strategy for enhancing heat transfer coefficients, offering considerable utility across diverse thermal processes. Predominantly, its applications span industries and technologies, encompassing the thermal development of photographic films, cooling of electronic components, processes within the food industry, and heat exchangers for aeronautical purposes. Further utilization has been documented in the drying of paper, cooling walls of external combustion engines, and in the regulation of temperatures in gas turbine components and photovoltaic cells. The essence of jet impingement cooling hinges on the intricate thermal dynamics that ensue when a high-velocity jet impinges upon a partial plate. This phenomenon is characterised by potent flow circulations, pronounced pressure gradients, and significant attenuation of local boundary-layers [1, 2].

Historically, scholarly attention has predominantly gravitated towards numerical and experimental evaluations pertaining to jet impingement cooling on heated flat surfaces. For instance, a numerical exploration of the efficacy of a confined impinging jet as a heat transfer medium was conducted by Manca et al. [3]. Within their research parameters, encompassing Re ranging between 5000 and 20000 and an impingement surface-to-jet spacing of 4-20, it was observed that the Nu exhibited minimal values towards the extremities of the target plate and peaked at the stagnation point. Concurrently, a surge in the Re was correlated with an elevation in $\overline{Nu}$. Their results further elucidated that, at a surface-to-jet distance of 10, heat transfer experienced an augmentation of up to 18%. Concurrently, a surge in Re was noted to necessitate an elevated pumping power. In a comprehensive numerical analysis spearheaded by Culun et al. [4], heat transfer dynamics of an air multi-nozzle array impingement on a smooth impinging plate

were systematically dissected. Both staggered and inline configurations were considered, employing two distinct nozzle geometries: square and circular. The impingement target surface was subjected to a uniform heat flux, and investigations spanned a Re spectrum of 5000 to 15000, with plate-to-jet spacing variables set at 2, 3, and 4 jet diameters. Pertinently, fluid outflow was analysed across three distinct configurations: a singular outlet, and dual and triple outlets in the outlet fluid regions. It was discerned that the Nu demonstrated a positive correlation with increasing Re. A pivotal observation was the superior heat transfer capabilities of square jets compared to their circular counterparts for a specified outflow configuration. Transitioning from a nozzle Re of 5000 to 10000 was associated with a substantial heat transfer enhancement, approximated at around 73%. Further complementing this domain of inquiry, Caggese et al. [5] undertook a dual approach, amalgamating both experimental and numerical methodologies, to understand the turbulent flow and thermal dynamics of fully-confined air jet impingement. Smooth surfaces were uniformly employed on both target (lower wall) and jet (upper wall) interfaces, facilitating the derivation of their individual local heat transfer coefficient profiles. Critical variables under scrutiny encompassed nozzle-to-target distances (ranging from 0.5 to 1.5 nozzle diameters) and nozzle Re, which varied between 16,500 and 41,800. An intriguing outcome was the escalating $\overline{Nu}$ of the target plate concomitant with rising nozzle Re. While the average and local Nu exhibited negligible variance as a function of impingement-to-jet spacings on an impinging flat plate, metrics for a jet-to-target spacing of merely 1 revealed optimal thermal enhancement. Consequently, compared to surfaces that experienced direct stagnation zones, the impingement target surface's heat transfer enhancement was measured to be approximately 40% diminished. In a comprehensive study orchestrated by Zhou et al. [6], the intricacies of flow field dynamics and thermal properties under the purview of air impingement jet at constrained spacings were exhaustively probed. The experimental setup incorporated both circular and swinging jets, each maintaining a jet length of 40 mm. The circular conduit was characterized by an outer diameter of 10 mm, an inner diameter of 13 mm, and a length of 200 mm. The variables of interest in their study encompassed impinging jet-to-target spacings, ranging from 0.5 to 3.0 jet diameters, and assorted coolant nozzle Re, spanning values of 5000, 10000, and 15000, applicable to both nozzle variants. From the ensuing data, it was deduced that the Nu exhibited an upswing corresponding to diminished spacings and escalating nozzle Re. Noteworthy was the superior thermal performance demonstrated by the sweeping jet when juxtaposed against its circular counterpart in the impingement precincts. Specifically, in the impingement domain, an enhancement in heat transfer of approximately 40% was observed with the sweeping jet in comparison to the circular iteration. A study by Sharif and Banerjee [7] numerically delved into the flow and thermal attributes exhibited on a heated flat target surface under the influence of a confined slot jet. With a designated impinging target length of 100 mm and a slot confined jet width of 6.2 mm, their analysis meticulously scrutinised the ramifications of target plate-to-air jet spacings of 6 and 8, encompassing a diverse spectrum of Re ranging from 5000 to 20000, as well as dimensionless target plate velocities oscillating between 0 and 2, all maintained at a steadfast impingement plate temperature of 338 K. It was discerned that the Nu escalated concomitantly with Re increments, particularly pronounced at static locations with minimal normalized plate velocities across all nozzle-to-impinging spacings. Furthermore, a conspicuous reduction in the average coefficient of skin friction was observed with escalating jet exit Re. Meanwhile, $\overline{Nu}$ amplified consistently across all normalized jet-to-target spacings. In a complementary vein, Huang [8] proffered a numerical exploration into the thermal dynamics on a heated surface facilitated by a confined axis-symmetric jet impinging. The study was premised on a radius geometrical configuration paired with a jet orifice diameter of 16 mm and 2 mm respectively. Key parameters like varied nozzle-to-target surface spacings and an array of Re were factored into their analysis. Consistent findings emerged for a gamut of jet Re, anchored between 5000 and 30,000, all harmonized under a uniform heat flux, albeit spanning an array of jet diameters between 1 and 5. A noteworthy revelation from their analysis pinpointed the impingement point region as the zenith of Nu concentrations. In tandem with this, $\overline{Nu}$, surged with the amplification of Re. A specific configuration, entailing a jet Re of 30,000 complemented by a target plate spacing of 2, manifested an $\overline{Nu}$ approximation of 15%.

Subsequent analyses have delved, both numerically and experimentally, into the intriguing interplay of jet impingement with dimpled and textured surfaces. A notable numerical exploration by Mondal and Singh [9] focused on the ramifications of a convex dimple on an impinging target plate, employing a solitary slot-jet. Their assessment underscored the efficacy of a staggered nine by nine matrix of hemispherical convex dimples, which manifested commendable thermal performance vis-à-vis an isothermal surface. Parameters such as a fixed nozzle-to-surface distance of 4, jet Re oscillating between 2750 and 11,000, a ratio of slot width to dimple diameter at 0.5, and a depth-to-diameter ratio of dimples pegged at 0.2 were systematically factored into their inquiry. It was elucidated that, under consistent nozzle-to-target proximities, the amplification of nozzle Re invariably led to an augmented Nu across both pristine and dimpled impinging arenas. Furthermore, the influence of Re appeared to be inconsequential on both anterior and posterior dimple localities. The culmination of their insights indicated a pronounced 50% surge in heat transfer efficacy in scenarios entailing dimples, juxtaposed against a conventional flat target plate. Corroborating this narrative, Wan et al. [10] embarked on a comprehensive numerical and experimental investigation into the thermal and flow dynamics endemic to cooling multi-jet front systems. They employed flat plates alongside textured plates, punctuated by both inline and staggered square pin fin topographies. These structured terrains

served as the subjects of impingement. Their analytical framework encompassed an examination of the implications stemming from variances in the Re of the cooling air jet, spanning a range from 15,000 to 35,000. Consistently, the $\overline{Nu}$ exhibited a propitious rise concomitant with the increment of nozzle Re. Notably, a marked 34.5% escalation in heat transfer enhancement was registered on the inline pin fin plate, juxtaposed against its flat plate counterpart. From an efficiency standpoint, the inline pin fin configuration demonstrably outstripped its staggered counterpart. Shukla et al. [11] presented a numerical study to delineate the influence of ribbed rough plates on heat and fluid flow characteristics under the aegis of an impinging slot-jet. Analyses were conducted for Re oscillating between 5500 and 20,000 and flow-to-impinging-surface distances of 4, 8, and 9.2. Within these parameters, it was observed that at a nozzle-to-impinging surface distance of 8 and a Re of 5500, the zenith of Nu values materialized in proximity to the stagnation zone on a ribbed plate. Significantly, the Nu metric was found to register augmented values when rib-embellished surfaces were deployed, juxtaposed against their smoother counterparts. In a complementary vein, Buzzard et al. [12] undertook an experimental foray to unravel the ramifications of plate roughness archetypes on target plates, employing an impingement cooling jet array. The paradigm of surface roughness under scrutiny was rectangular, coalesced with an expansive rectangular pin. Conjoint analyses with diminutive rectangular roughness arrays and larger-pin combinations were undertaken. The experimental framework was buttressed by air cooling, with the nozzle Re spanning a gamut from 900 to 11,000. A noteworthy revelation was that surfaces festooned with minute rectangular roughness manifested superior Nu values at lower Re, whilst those graced with a juxtaposition of diminutive combinations and expansive rectangular roughness excelled at heightened Re. Furthermore, an elevation in the stature of petite roughness invariably translated into a discernible amplification in the Nu metric across the entire spectrum of nozzle Re. Xu et al. [13] undertook a rigorous numerical investigation to probe into the entropy generation and heat transfer dynamics of a slot air jet impinging on a roughened plate, which embodied a sinusoidal wave model. In this exploration, parameters were varied, encompassing Re oscillating between 2738 and 10,952 and jet-to-impingement plate spacings ranging from 4 to 8. It was discerned that, when juxtaposed against a planar surface, the roughened surface exhibited a markedly augmented thermal enhancement. Concurrently, it was observed that with escalating Re, both the $\overline{Nu}$ and the concomitant thermal and viscous entropy generation manifested an upward trajectory. Poignantly, when benchmarked against a planar surface, the $\overline{Nu}$ associated with the rough surface was ascertained to surge by an approximate magnitude of 40%.

From a survey of prior literature, it is evident that a substantial focus has been directed towards the implementation of square and circular jet impingement on roughened target surfaces, a technique known to enhance heat transfer performance. In light of these findings, the exploration of slot-jet impingement, particularly when interfaced with a heated surface adorned with wing ribs, emerges as a novel avenue. This approach not only exhibits potential in refining heat transfer dynamics but also in modulating entropy generation attributes. Such advancements may offer a refreshing paradigm shift from conventional methodologies employed in the cooling of electronic components.

2 Numerical Simulation

2.1 Problem Description

A two-dimensional model, representing a confined impinging orifice-jet onto a target plate, is illustrated in Figure 1. Specific parameters for this configuration are delineated as follows: The two-dimension model of confined impinging orifice-jet on a target plate is demonstrated in Figure 1. The target plate length (L) is 110 mm, the distance between the target plate and orifice jet (H) is 10 mm, the orifice-jet width (Z) is 10 mm, the rib length (D) is 10 mm, various heights of rib (A) are (0.5, 1, 1.5, and 2 mm), and a difference in the distance from the rib-to-the stagnation point (B) is (10, 20, and 30 mm), and study state, incompressible, and turbulent flow were taken as assumptions in this investigation. Additionally, a uniform, constant heat flux of 8000 $\mathrm{W/m^2}$ is applied to the bottom surface, which is the target plate. Water is chosen as the working fluid. The working fluid's thermophysical properties at 298 K are thermal conductivity (k_f) of 0.6094 W/(m.k), the density (ρ) of 997.9 $\mathrm{kg/m^3}$, specific heat (C_p) of 4144 J/(kg.k) and dynamic viscosity (μ) of 0.001 kg/(m.s) [14].

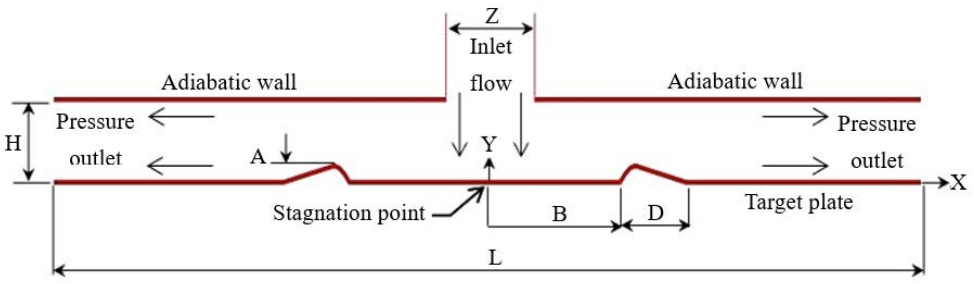

Figure 1. Geometrical model of confined impinging orifice-jet on the target plate

2.2 Governing Equations

For analysis, the governing equations, articulated in Cartesian coordinates, are as delineated below [15]:
Continuity equation:

$$\frac{\partial u}{\partial x}+\frac{\partial v}{\partial y}=0 \tag{1}$$

u-momentum equation:

$$\begin{aligned}\frac{\partial}{\partial x}(\rho uu)+\frac{\partial}{\partial y}(\rho uv)=&-\frac{\partial p}{\partial x}+\frac{\partial}{\partial x}\left[\mu_{eff}\frac{\partial u}{\partial x}\right]+\frac{\partial}{\partial y}\left[\mu_{eff}\frac{\partial u}{\partial y}\right]\\&+\frac{\partial}{\partial x}\left[\mu_{eff}\frac{\partial u}{\partial x}-\frac{2}{3}\rho k\right]+\frac{\partial}{\partial y}\left[\mu_{eff}\frac{\partial v}{\partial x}\right]\end{aligned} \tag{2}$$

v-momentum equation:

$$\begin{aligned}\frac{\partial}{\partial x}(\rho uv)+\frac{\partial}{\partial y}(\rho vv)=&-\frac{\partial p}{\partial y}+\frac{\partial}{\partial x}\left[\mu_{eff}\frac{\partial v}{\partial x}\right]+\frac{\partial}{\partial y}\left[\mu_{eff}\frac{\partial v}{\partial y}\right]\\&+\frac{\partial}{\partial x}\left[\mu_{eff}\frac{\partial u}{\partial y}\right]+\frac{\partial}{\partial y}\left[\mu_{eff}\frac{\partial v}{\partial y}-\frac{2}{3}\rho k\right]\end{aligned} \tag{3}$$

Energy equation:

$$\frac{\partial}{\partial x}(\rho uT)+\frac{\partial}{\partial y}(\rho vT)=\frac{\partial}{\partial x}\left[\left(\frac{\mu}{Pr}+\frac{\mu_t}{Pr_t}\right)\frac{\partial T}{\partial x}\right]+\frac{\partial}{\partial y}\left[\left(\frac{\mu}{Pr}+\frac{\mu_t}{Pr_t}\right)\frac{\partial T}{\partial y}\right] \tag{4}$$

In the present study, the turbulent-dynamic viscosity is computed using the Launder and Sharma ($\mathrm{k}-\varepsilon$) turbulence model. Therefore, the expression for turbulent eddy viscosity is given as [16]:

$$\mu_t=C_\mu f_\mu \rho\frac{k^2}{\varepsilon} \tag{5}$$

Turbulent kinetic energy (k) equation:

$$\frac{\partial}{\partial x}(\rho uk)+\frac{\partial}{\partial x}(\rho vk)=\frac{\partial}{\partial x}\left[\Gamma_k\frac{\partial k}{\partial x}\right]+\frac{\partial}{\partial y}\left[\Gamma_k\frac{\partial k}{\partial y}\right]+P_k-\rho\left(\varepsilon+\varepsilon_w\right) \tag{6}$$

Here ε_w represents that the dissipation rate at the target plate, as well as it has been given by:

$$\varepsilon_w=2\frac{\mu}{\rho}\left[\left(\frac{\partial\sqrt{k}}{\partial x}\right)^2+\left(\frac{\partial\sqrt{k}}{\partial y}\right)^2\right] \tag{7}$$

Turbulent kinetic energy dissipation (ε) equation [16]:

$$\begin{aligned}\frac{\partial}{\partial x}(\rho u\varepsilon)+\frac{\partial}{\partial y}(\rho v\varepsilon)=&\frac{\partial}{\partial x}\left[\Gamma_\varepsilon\frac{\partial\varepsilon}{\partial x}\right]+\frac{\partial}{\partial y}\left[\frac{\partial\varepsilon}{\partial y}\right]\\&+\left(C_1f_1P_k-\rho C_2f_2\varepsilon\right)\frac{\varepsilon}{k}+\emptyset_\varepsilon\end{aligned} \tag{8}$$

where,

$$\emptyset_\varepsilon=2\mu_t\frac{\mu}{\rho}\left[\left[\left(\frac{\partial^2u}{\partial x^2}\right)^2+\left(\frac{\partial^2v}{\partial x^2}\right)^2\right]+2\left(\frac{\partial^2u}{\partial x\partial y}\right)^2+2\left(\frac{\partial^2v}{\partial x\partial y}\right)^2+\left(\frac{\partial^2v}{\partial y^2}\right)^2\right] \tag{9}$$

In the above equations, the term P_k signifies the production rate of turbulent kinetic energy. This can be articulated as:

$$P_k = \mu_t \left\{ 2 \left[\left(\frac{\partial u}{\partial y} \right)^2 + \left(\frac{\partial v}{\partial x} \right)^2 \right] + \left(\frac{\partial u}{\partial y} + \frac{\partial v}{\partial x} \right)^2 \right\} - \frac{2}{3} \rho k \left(\frac{\partial u}{\partial x} + \frac{\partial v}{\partial y} \right) \tag{10}$$

For the empirical constants and the turbulent Prandtl number used above, their definitions are as follows [16]:

$$\sigma_k = 1.0, \sigma_\varepsilon = 1.3, Pr_t = 0.9, C_1 = 1.44, C_2 = 1.92, C_\mu = 0.09 \tag{11}$$

The turbulent jet Re and the wall-damping functions were determined in accordance with the following [17]:

$$f_1 = 1.0 \tag{12}$$

$$f_2 = 1 - 0.3 \exp\left(-Re_T^2\right) \tag{13}$$

$$f_\mu = \exp\left[\frac{-3.4}{\left(1 + 0.02 Re_T\right)^2} \right] \tag{14}$$

$$Re_T = \frac{\rho}{\varepsilon} \frac{k^2}{\mu} \tag{15}$$

2.3 Boundary Conditions

To solve the governing equations presented earlier, specific boundary conditions were applied as delineated by study [18]. These conditions were chosen to address challenges encountered in electronic devices, facilitating simulations that aid in preempting complications during design stages.

At the orifice-jet inlet:

$$v = v_{in}, u = 0, T = T_{in}, k = k_{in} = \frac{2}{3} \left(0.05 v_{in}\right)^2, \varepsilon = \varepsilon_{in} = \frac{c_\mu^{3/4} k_{in}^{3/2}}{(0.07 Z)} \tag{16}$$

$$\frac{\partial u}{\partial \xi} = 0, \frac{\partial v}{\partial \xi} = 0, \frac{\partial T}{\partial \xi} = 0, \frac{\partial k}{\partial \xi} = 0, \frac{\partial \varepsilon}{\partial \xi} = 0 \tag{17}$$

At the upper plate (adiabatic wall)

$$u = 0, v = 0, k = 0, \varepsilon = 0, \quad \left. \frac{\partial T}{\partial \eta} \right|_p = 0 \tag{18}$$

At the lower target plate

$$u = 0, v = 0, k = 0, \varepsilon = 0, \quad \left. \frac{\partial T}{\partial \eta} \right|_p = -\frac{q_p}{k_f} \tag{19}$$

Upon discretization of the governing equations, fluid flow and temperature fields were analyzed. The resultant equations facilitated the calculation of both local and average Nu. The local Nu, representing the ratio of convective to conductive heat transfer at a boundary on the target surface, was derived as [19]:

$$Nu = \frac{Z}{k_f} \frac{q_p}{(T_p - T_b)} \tag{20}$$

Here, T_p represents that the temperatures distribution along target plate and T_b signifies the bulk fluid temperature that can be computed as follows [19]:

$$T_b = \frac{\iint_A \rho v C_p T dA}{\iint \rho v C_p dA} \tag{21}$$

The calculation of the average Nu includes the integration of the (Nu) on an identified target surface:

$$\overline{Nu} = \frac{1}{L}\int_0^L Nu \; dx \tag{22}$$

The thermal-hydraulic performance, represented as PEC, describes the ratio between the improvements in Nu and friction factor. It is expressed as [20]:

$$PEC = \frac{\left(\overline{Nu}_r/\overline{Nu}_s\right)}{\left(f_r/f_s\right)^{1/3}} \tag{23}$$

Here, f indicates the friction factor that can be calculated as follows [20]:

$$f = \Delta p \frac{Z}{L}\frac{2}{\rho u^2} \tag{24}$$

2.4 Entropy Generation Analysis

In addition, the two dimensional average entropy generations of the viscous dissipation $\overline{\mathrm{S}}_{vi}$ and heat transfer (thermal) $\overline{\mathrm{S}}_{th.}$ along target surface can be given as follows [21]:

$$\bar{S}_{vi.} = \frac{\mu}{T}\left\{2\left[\left(\frac{\partial u}{\partial x}\right)^2 + \left(\frac{\partial v}{\partial y}\right)^2\right] + \left(\frac{\partial u}{\partial y} + \frac{\partial v}{\partial x}\right)^2\right\} \tag{25}$$

$$\bar{S}_{th.} = \frac{k_f}{T^2}\left[\left(\frac{\partial T}{\partial x}\right)^2 + \left(\frac{\partial T}{\partial y}\right)^2\right] \tag{26}$$

Furthermore, the averages of the viscous and thermal entropy generations have been defined as the dimensionless number by utilizing thermal conductivity and slot-jet width as follows:

$$\left(\bar{S}_{vi.}\right)_z = \bar{S}_{vi.} \times \frac{Z^2}{k_f} \tag{27}$$

$$\left(\bar{S}_{th.}\right)_z = \bar{S}_{th.} \times \frac{z^2}{k_{\mathrm{f}}} \tag{28}$$

Also, the dimensionless number of the average total entropy generation can be presented by:

$$\left(\bar{S}_{\text{total}}\right)_Z = \left(\bar{S}_{th.}\right)_Z + \left(\bar{S}_{vi.}\right)_Z \tag{29}$$

2.5 Numerical Approach

In the study at hand, the FVM was employed for discretizing the governing equations. For the convection and diffusion terms present within these equations, the second order upwind and central differencing methods were respectively applied. The SIMPLE-algorithm, renowned for its efficacy in solving the Navier-Stokes equations, was utilized to simulate the pressure field. This algorithm has been extensively referenced in literature for addressing a multitude of heat transfer and fluid flow challenges [22, 23].

The computational grid for this study was constructed using two Poisson equations, as depicted in Figure 2. The under-relaxation approach, a method pivotal for enhancing computational stability, especially in steady-state analyses where initial iterations bear significance, was integrated to optimize convergence performance for all variables. Consequently, a convergence criterion for each dependent variable was established at (1.0×10^{-5}).

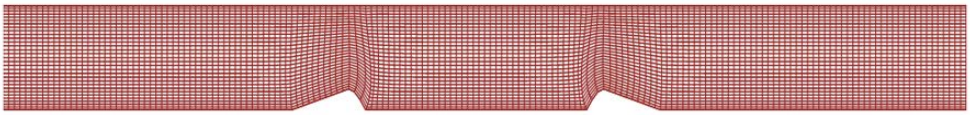

Figure 2. Computational mesh for the present study

2.6 Numerical Code Validation and Grid Optimization Check

For the validation of the numerical methodology adopted, the friction factor of an impinging confined jet on a flat impingement surface was ascertained. This factor was then juxtaposed with results derived from Buonomo et al. [24]. As illustrated in Figure 3, a commendable agreement between both sets of results was observed. The friction factor essentially delineates the pressure loss experienced by a fluid within a conduit, attributable to its interactions with the conduit's target surfaces. The significance of investigating this particular factor lies in its applicability to various applications, especially given its precision and capacity to elucidate behavioral changes across a spectrum of Re.

For the purpose of mesh optimization, a spectrum of grid densities, including (361×51, 461×61, 561×71, 661×81, 761×101), was subjected to examination. Figure 4 displays the friction factor mapped across these varying grid densities, maintaining a rib height of 2 mm, a distance of 20 mm from the rib to the stagnation point, and jet Re oscillating between 3000 and 8000. Upon scrutiny, the grid density of 661×81, comprising 661 grid nodes longitudinally (X-direction) and 81 latitudinally (Y-direction), was discerned to facilitate optimal grid convergence.

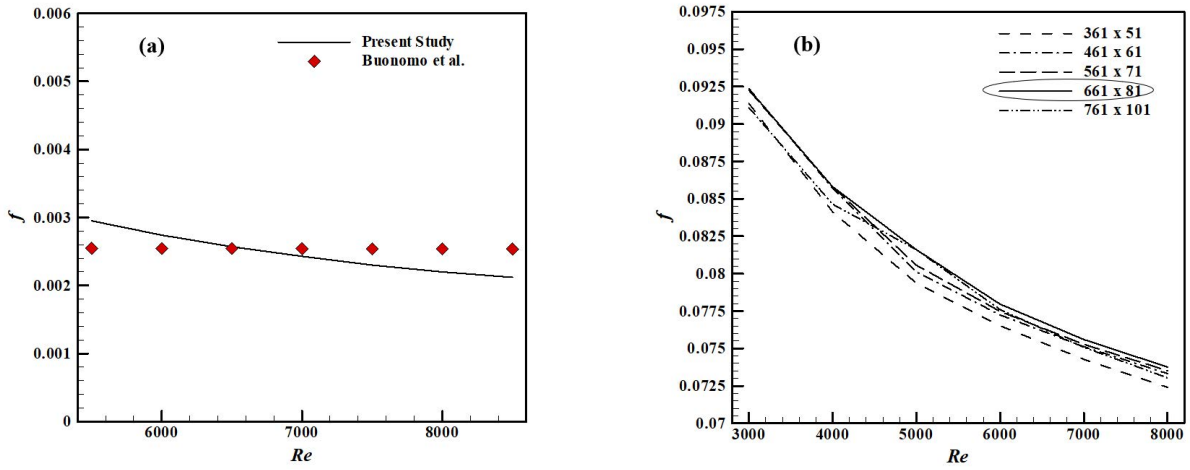

(a) (b)

Figure 3. Comparison of (a) Friction factor for the present study with numerical investigation of Buonomo et al. [24], (b) Friction factor vs. jet Re for various grid densities at a= 2 mm and d=20 mm

3 Results and Discussion

In this chapter, influences of varying parameters on thermal dynamics, fluid flow, and entropy generation are elucidated. Parameters such as the jet Re, ranging from Re=3000 to 8000, the wing rib height, spanning values of a=0.0, 0.5, 1, 1.5, and 2 mm, and the spacing between the wing rib and the stagnation point, set at intervals of d=10, 20, and 30 mm, have been assessed. Moreover, contours illustrating velocity, temperature, and entropy generation have been depicted for the right half of the domain, predicated on the symmetrical nature of the physical field about the y-axis.

3.1 Implications of Varying Rib Heights

Velocity contours corresponding to diverse rib heights, given a stagnation point and wing rib spacing of 10 mm with a jet Re of 5000, are depicted in Figure 4. These contours accommodate both the wing rib shape and a smooth target plate scenario, absent of ribs. When fluid is introduced via the slot jet on the left facet of the upper confined plate, subsequently impinging on the rib-less target plate (a=0.0), a distinct primary vortex formation near the slot-jet is observed. This vortex arises from the prevailing shear force engendered by the jet's high velocity. Introduction of a rib on the impingement target plate profoundly modulates the primary flow vortex near the upper confinement surface, manifesting in a notable reduction in both the vortex's intensity and dimensions.

The existence of the primary vortex, though detrimental to heat transfer on the confined surface (adiabatic wall), induces an elevation in the pressure drop by amplifying reverse fluid dynamics. Consequently, the mitigation in the primary vortex's magnitude and extent results in a pressure drop decrement. Furthermore, a secondary-clockwise vortex downstream of ribs with varied shapes on the target plate emerges. An amplification in the rib height escalates the intensity and dimensions of this secondary vortex, fostering enhanced fluid flow mixing and subsequent heat transfer augmentation. Moreover, with the ascent of the rib height, the gap between the upper and lower plates contracts, accelerating fluid velocity at the channel's nucleus. However, it's pertinent to note that the thermal performance ratio is enhanced with increasing rib heights. A pinnacle in the secondary flow vortex's magnitude and intensity, observed at a=2 mm, signifies an optimal heat transfer elevation.

Temperature contours, exhibited in Figure 5, correspond to a jet Re of 5000 and a 10 mm rib spacing, exploring a spectrum of rib heights. For a=0.0, a minimal thermal boundary layer thickness is discerned at the stagnation point, escalating in its extent as one traverses along the impinging target plate. An expansion in the vortex domain is witnessed with surging rib heights, catalyzing the intermixing of cold core channel water with the warmer flow at the target plate.

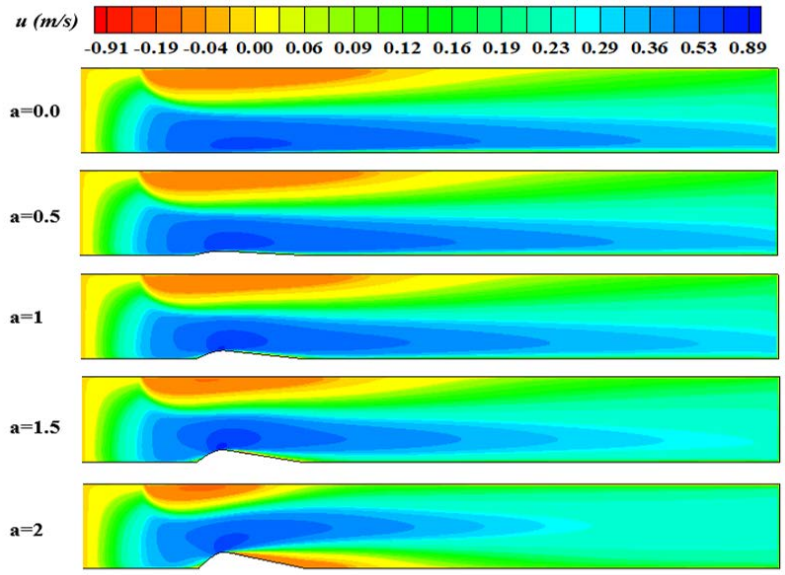

Figure 4. Velocity contours for different rib heights at jet Re=5000 and d=10 mm

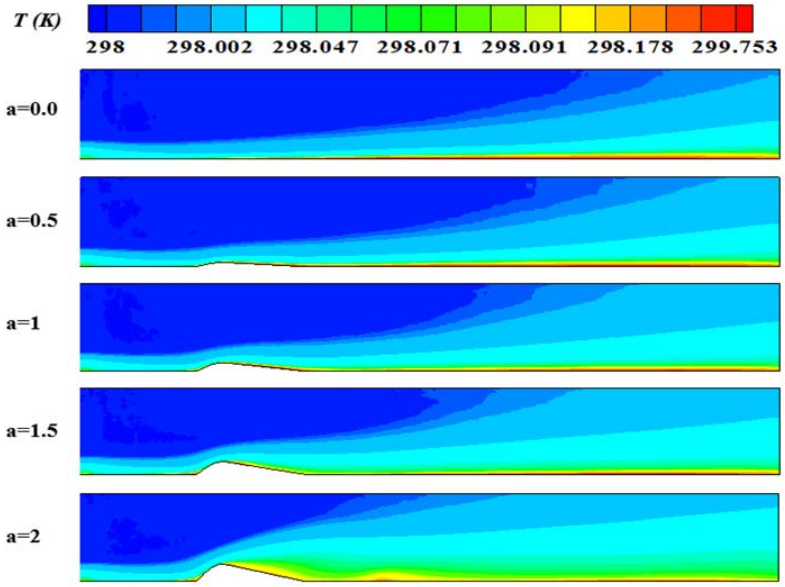

Figure 5. Temperature contours for different rib heights at jet Re=5000 and d=10 mm

In Figure 6, total entropy-generation contours at a jet Re of 5000, and a rib location of 10 mm across various rib heights are presented. At the impingement point and on the rib surface, the peak entropy generation was identified, which subsequently diminished in intensity downstream of the rib. Increasing rib heights exhibited an amplification in average total entropy generation, attributable to the intensified influence of thermal and viscous dissipation irreversibilities.

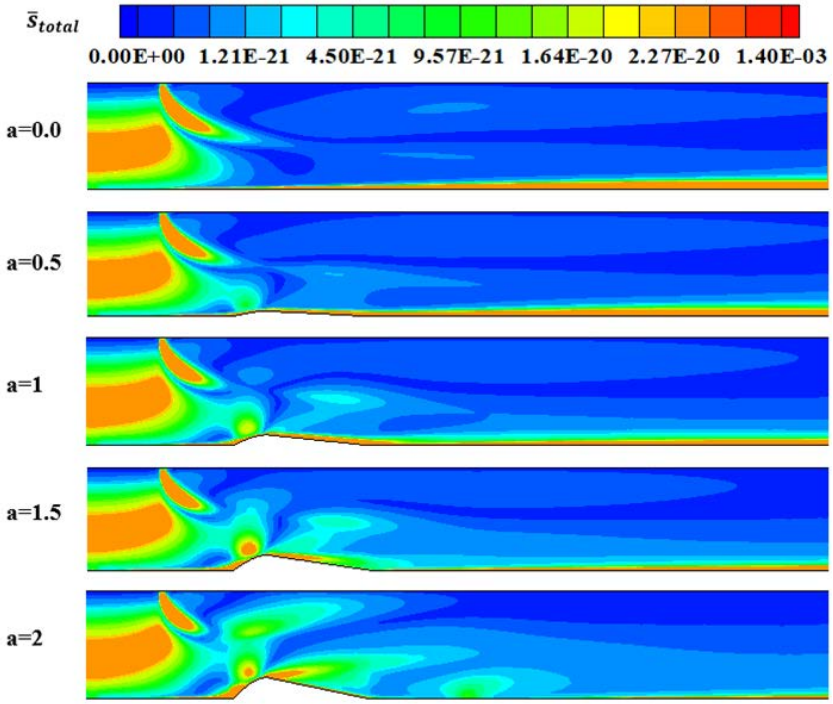

Figure 6. Total entropy generation contours for various rib heights at jet Re=5000 and d=10 mm

The interrelation between the average Nu and jet Re, for different rib heights at d=10 mm, is expounded in subgraph (a) of Figure 7. A salient observation from the figure is the substantial modulation of the average Nu by the jet Re and rib height variations. At specific rib heights, the escalation of the jet Re corresponds to an increased average Nu, a phenomenon ascribed to the elevated temperature gradient at the bottom impingement target surface. Concurrently, for a fixed jet Re, an increment in the rib height accentuates the average Nu. This increment is attributed to the expansion of vortex regions, fostering enhanced fluid flow mixing and consequent thermal rate elevation. Among the examined parameters, the paramount average Nu was detected at a=2 mm. These observations resonated with numerical studies conducted by Buzzard et al. [12] and Xu et al. [13].

Depicted in subgraph (b) of Figure 7 is the variation of the pressure drop with the jet Re at d=10 mm across an array of rib heights. Pressure drops were observed to accentuate with the increasing jet Re for all rib heights, a consequence of velocity gradients. In comparison to various rib heights, the most negligible pressure drop was discerned at a=0.0. An amplification in the rib height led to an escalated pressure drop, driven by the augmented size and intensity of the flow vortex zone. Notably, the apical pressure drop was manifested at a jet Re of 8000 for a=2 mm, when juxtaposed with other heights.

The subgraph (c) of Figure 7 encapsulates the variations in the average total entropy generation with the jet Re at d=10 mm across the spectrum of rib heights. Across all rib heights, an ascension in the average total entropy generation was evident with the increment of the jet Re. The elevation in the total average entropy generation with rib height was discerned, stemming from the growing irreversibilities of viscous dissipation and heat transfer. A distinct observation was the peak average total entropy generation manifested at a=2 mm [13].

In subgraph (d) of Figure 7, the variation of the thermal-hydraulic performance (PEC) with respect to the Re at d=10 mm for different rib heights is delineated. It is discernible from the data that the rib heights exert a pronounced influence on the thermal-hydraulic performance. At a=2 mm, across the vast majority of the jet Re spectrum (with the exception of jet Re=3000), the zenith of the performance factor was observed. This observation implies that the beneficial ramifications of enhanced heat transfer overwhelmingly outweigh the detrimental effects associated with the pressure drop penalty.

For Re exceeding 5000, the PEC at a=1 mm was found to register the minimal value. Moreover, the apogee of the PEC values, amounting to 1.682, was identified at a=2 mm for a jet Re of 3000.

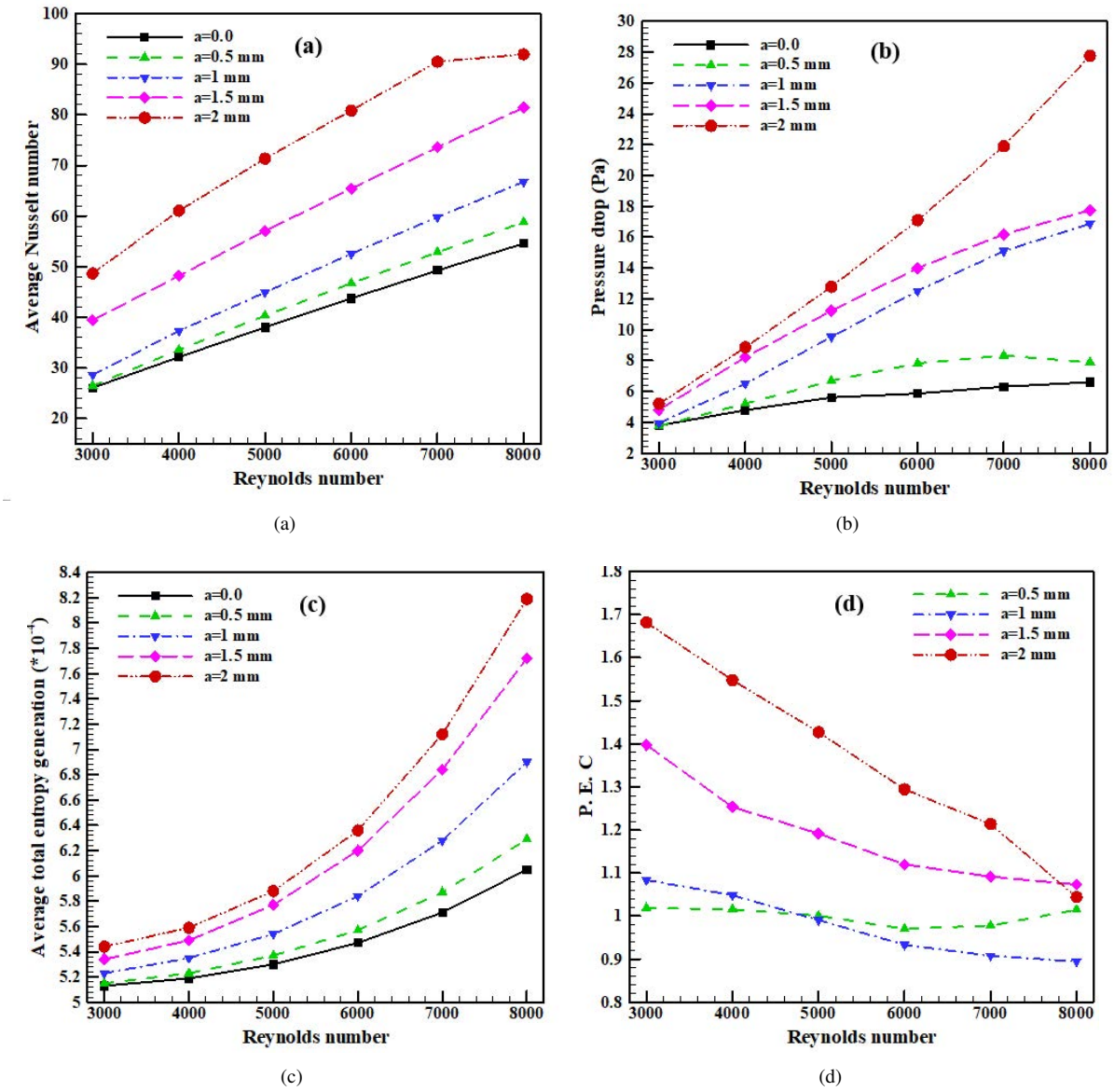

Figure 7. Variation of (a) average Nu, (b) pressure drop, (c) total average entropy generation, (d) thermal-hydraulic performance versus jet Re for various rib heights at d=10 mm

3.2 Implications of Varying Rib Locations

In Figure 8, the ramifications of modulating the distance between the rib and the impingement point (d=10, 20, and 30 mm) on the velocity contours, given a jet Re=7000 and a=2 mm, are elucidated. A distinct perturbation in velocity is ascertained based on the rib's positioning. For d=10 mm, the inverse re-circulatory fluid flow manifesting downstream of the rib remains relatively subdued. Concomitantly, the influence of the rib on the magnitude and intensity of the primary re-circulation at the confined wall remains minimal. When transitioning to d=20 mm, emergent secondary re-circulation domains are identified downstream of the rib, and a marked escalation in the primary vortex's dimensions becomes evident, potentially attenuating the heat transfer enhancement. A pronounced amplification of the primary vortex dimensions is discerned for d=30 mm, indicating that elevating the rib's distance invariably augments the primary vortex size.

Temperature contours corresponding to assorted rib positions, under the conditions of jet Re=7000 and a=2 mm, are presented in Figure 9. The post-rib re-circulation domain culminates in a comparatively leaner thermal boundary layer upstream, as contrasted with its downstream counterpart. Within the downstream re-circulatory area, as the interstitial distance between the impingement point and rib grows, an inflation in the thermal boundary layer's thickness is observed. A pronounced thermal gradient in this vicinity elucidates the most attenuated thermal boundary layer dimensions proximate to the impingement locus.

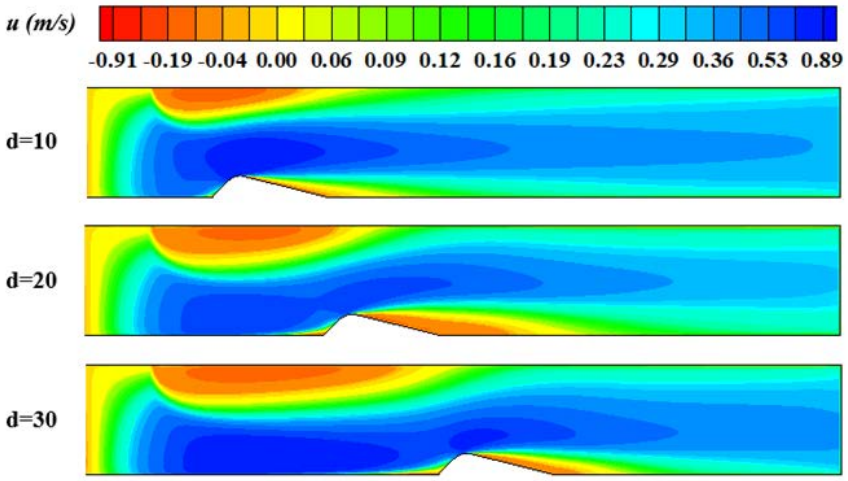

Figure 8. Velocity contours for different rib locations at jet Re=7000 and a=2 mm

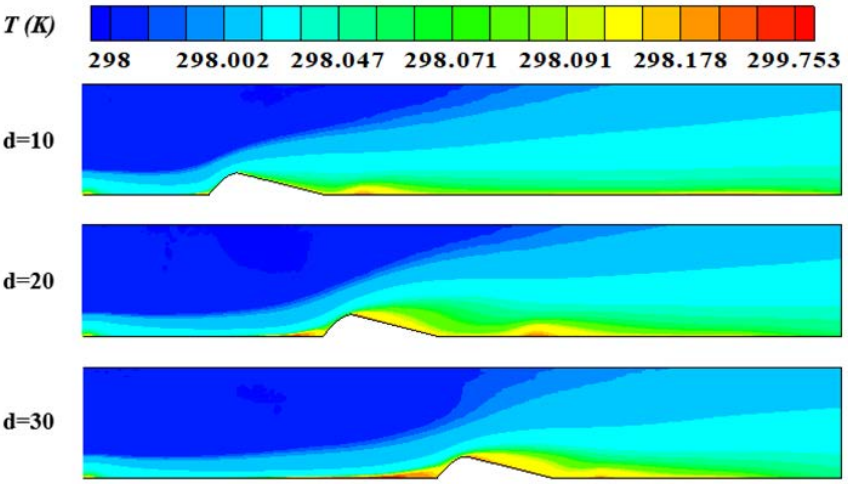

Figure 9. Temperature contours for different rib locations at jet Re=7000 and a=2 mm

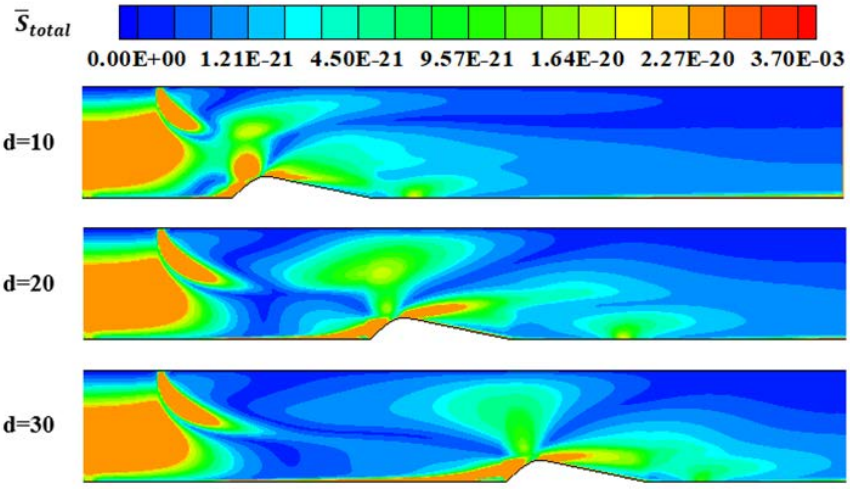

Figure 10. Total entropy generation contours for different rib locations at jet Re=7000 and a=2 mm

The total entropy generation contours, correlating with an array of rib proximities (d=10, 20, and 30 mm) at jet Re=7000 and a=2 mm, are showcased in Figure 10. The entropy generation palpably fluctuates based on the rib-to-impingement point distance. The apical entropy generation values are registered adjacent to the impingement

region, a phenomenon attributed to the acute temperature gradient therein. Owing to extant re-circulation domains, entropy generation upstream of the rib surpasses that of its downstream. Moreover, the zenith of entropy generation materializes at d=10 mm, and a subsequent decline is witnessed with incrementing rib proximities.

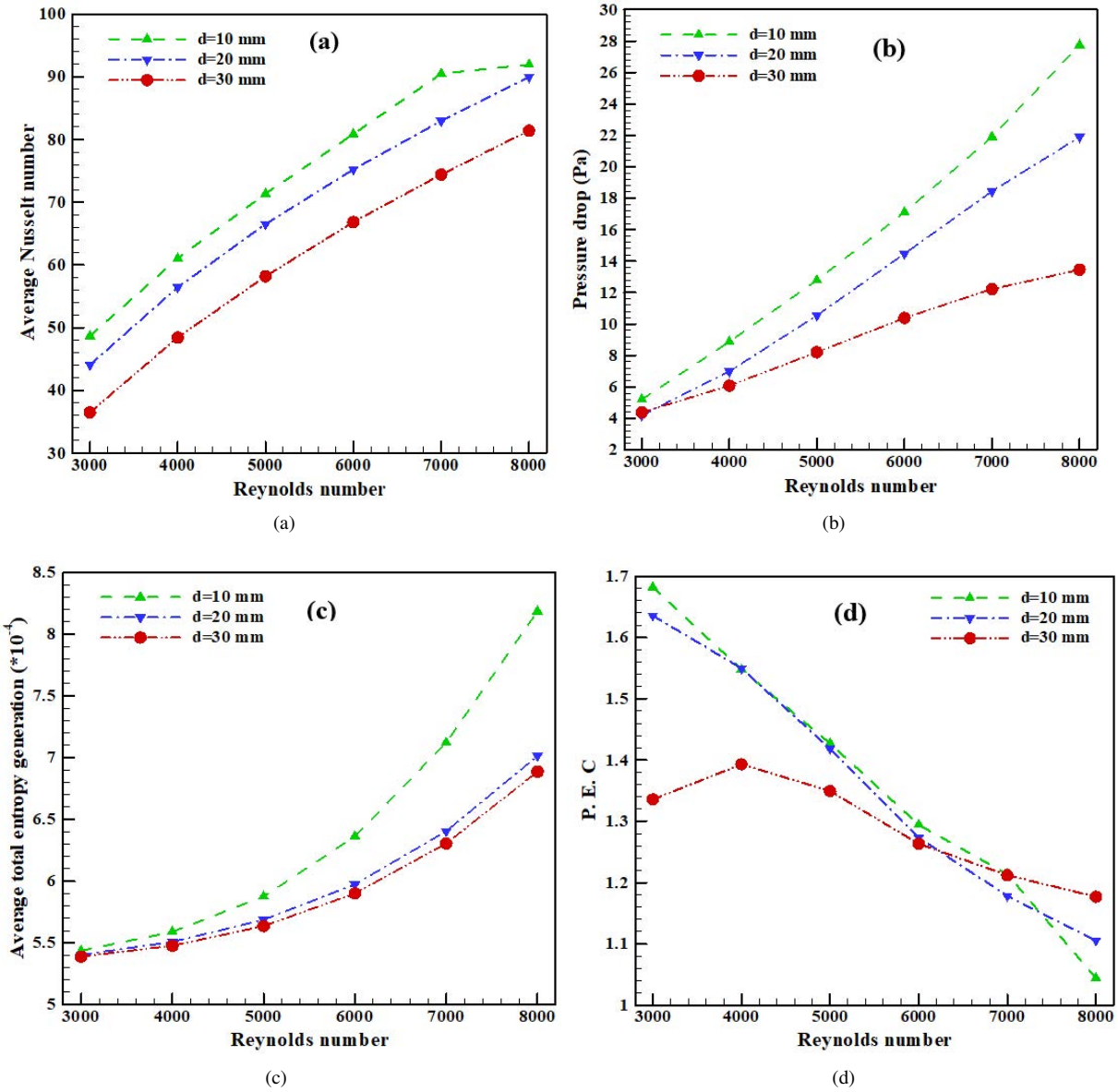

Figure 11. Variation of (a) average Nu, (b) pressure drop, (c) total average entropy generation, (d) thermal-hydraulic performance versus jet Re for various rib locations at a=2 mm

In subgraph (a) of Figure 11, an exploration of the average Nu against jet Re at a=2 mm is presented. An amplification in the average Nu was observed with an escalating jet Re, though this augmentation appears to recede as the rib's position extends outward. Correlating these findings with the velocity contours depicted in Figure 8, the proximity of d=10 mm between the rib and impingement point manifests the least pronounced primary re-circulation region proximate to the slot-jet at the confined plate. Moreover, the enhanced fluid flow mixing at this proximity culminates in superior heat transfer relative to other demarcated regions. A conspicuously subdued fluid flow mixing at d=30 mm aligns with diminished heat transfer, attributable to the expanded dimensions of the primary re-circulation, dwarfing its intensity.

The pressure differential in relation to jet Re at a=2 mm is depicted in subgraph (b) of Figure 11. A discernible rise in the pressure drop was observed with an incremented jet Re across all rib proximities. Furthermore, a contraction in rib proximity appeared to exacerbate this pressure surge, presumably due to the intensified flow disruptions as the rib approaches the impingement point. These observations are underscored by the velocity contours from Figure 8, elucidating the rib's influence on the primary re-circulation's magnitude and intensity near the slot-jet at the adiabatic

wall for d=10 mm. Evidently, a maximum reverse fluid flow is realized at this proximity.

The subgraph (c) of Figure 11 sheds light on the variation in the average entropy generation across different rib proximities at a=2 mm for varied jet Re. Across the entire spectrum of rib locations, an ascent in the overall average entropy generation was noted with the magnification of the Re. The influence of the distances between the rib and the impingement point on the overall entropy generation seems marginal at lower Re (jet $Re < 4000$), but this impact becomes more palpable as the Re escalates. A retreating rib location correlates with a surge in the average total entropy generation, a phenomenon underpinned by the interplay between primary and secondary zones proximate to the confined wall and the impinging target plate, respectively.

Lastly, the subgraph (d) of Figure 11 provides insights into the hydro-thermal performance (PEC) dynamics against jet Re at a=2 mm across an array of rib distances. It became evident that the rib proximities profoundly modulate the PEC. For d=10 and 20 mm, the PEC appears to wane as the jet Re augments, yet for d=30 mm, an initial elevation in PEC is detected at lower Re (jet $Re < 4000$), followed by a descent for higher values, presumably due to a modulated pressure drop relative to the heat transfer enhancement at this extended proximity. The peak PEC value, recorded as 1.68, coincided with the least jet Re for a distance of d=10 mm, contrasting with the trough value of PEC, denoted as 1.044, at the zenith of the jet Re for this specific distance.

4 Conclusions and Future Works

The characteristics of fluid flow, thermal dynamics, and entropy generation linked with confined slot-jet impingement were explored numerically. In an effort to discern their influence, two wing ribs of varied dimensions and positions were integrated onto the target surface. These configurations were subsequently juxtaposed against a rib-less, smooth impinging surface to ascertain the consequential alterations in fluid flow, heat transfer, and entropy fields. Utilizing the FVM, the governing equations were addressed based on the SIMPLE-algorithm. The predominant objective was to discern the optimal conditions for heat transfer and entropy generation enhancements through rib incorporations on the hot surface, when compared against a conventional horizontal flow channel.

From the analysis, several observations were made:

(1) As the jet Re escalates, corresponding increments in the average Nu, pressure drop, and total entropy generation are discerned.

(2) Elevated rib heights directly correlated with increased average Nu, pressure drop, average total entropy generation, and thermal-hydraulic performance.

(3) Diminishing distances between the impingement point and the ribs engendered a rise in the average Nu, pressure drop, and total entropy generation.

(4) The zenith of the thermal-hydraulic performance, approximately 1.68, was observed at a jet Re of 3000, with a rib positioning of 10 mm and a rib elevation of 2 mm.

Collectively, these findings advocate for the utility of slot-jet impingement supplemented with ribs on the heated surface. Specifically, a rib height of 2 mm, combined with a minimal distance between the ribs and the stagnation point, appears to offer superior outcomes in terms of cooling, suggesting potential applications in electronic component design.

In light of these findings, future avenues for exploration have been delineated:

(1) A meticulous numerical examination of the slot-jet width's impact on entropy generation and thermal enhancements is warranted.

(2) A comprehensive study delving into multi-slot jet impingement and its implications on heat transfer and fluid dynamics on rib-augmented heated target surfaces appears promising.

Data Availability

The data used to support the findings of this study are available from the corresponding author upon request.

Conflicts of Interest

The authors declare no conflict of interest.

References

[1] M. Amjadian, H. Safarzadeh, M. Bahiraei, S. Nazari, and B. Jaberi, "Heat transfer characteristics of impinging jet on a hot surface with constant heat flux using Cu_2O–water nanofluid: An experimental study," *Int. Commun. Heat Mass Transf.*, vol. 112, p. 104509, 2020. https://doi.org/10.1016/j.icheatmasstransfer.2020.104509

[2] R. Ekiciler, M. Çetinkaya, and K. Arslan, "Effect of shape of nanoparticle on heat transfer and entropy generation of nanofluid-jet impingement cooling," *Int. J. Green Energy*, vol. 17, no. 10, pp. 555–567, 2020. https://doi.org/10.1080/15435075.2020.1739692

[3] O. Manca, P. Mesolella, S. Nardini, and D. Ricci, "Numerical study of a confined slot impinging jet with nanofluids," *Nanoscale Res. Lett.*, vol. 6, no. 1, pp. 1–16, 2011.

[4] P. Culun, N. Celik, and K. Pihtili, "Effects of design parameters on a multi jet impinging heat transfer," *Alexandria Eng. J.*, vol. 57, no. 4, pp. 4255–4266, 2018. https://doi.org/10.1016/j.aej.2018.01.022

[5] O. Caggese, G. Gnaegi, G. Hannema, A. Terzis, and P. Ott, "Experimental and numerical investigation of a fully confined impingement round jet," *Int. J. Heat Mass Transf.*, vol. 65, pp. 873–882, 2013. https://doi.org/10.1016/j.ijheatmasstransfer.2013.06.043

[6] W. Zhou, L. Yuan, Y. Liu, D. Peng, and X. Wen, "Heat transfer of a sweeping jet impinging at narrow spacings," *Exp. Therm. Fluid Sci.*, vol. 103, pp. 89–98, 2019.

[7] M. Sharif and A. Banerjee, "Numerical analysis of heat transfer due to confined slot-jet impingement on a moving plate," *Appl. Therm. Eng.*, vol. 29, no. 2-3, pp. 532–540, 2009. https://doi.org/10.1016/j.applthermaleng.2008.03.011

[8] J. B. Huang, "Numerical study of a confined axisymmetric jet impingement heat transfer with nanofluids," *Eng.*, vol. 5, no. 1, pp. 69–74, 2013. https://doi.org/10.4236/eng.2013.51b013

[9] R. Mondal and D. Singh, "Numerical study on single slot jet impingement on hemispherical convex dimple surface," in *ICTEA: International Conference on Thermal Engineering*, 2019.

[10] C. Wan, Y. Rao, and P. Chen, "Numerical predictions of jet impingement heat transfer on square pin-fin roughened plates," *Appl. Therm. Eng.*, vol. 80, pp. 301–309, 2015. https://doi.org/10.1016/j.applthermaleng.2015.01.053

[11] A. Shukla, A. Dewan, and B. Srinivasan, "Computational study of turbulent slot jet impingement on a ribbed surface," in *Proceedings of the 6th International and 43rd National Conference on Fluid Mechanics and Fluid Power*, 2016, pp. 8–10.

[12] W. Buzzard, Z. Ren, P. Ligrani, C. Nakamata, and S. Ueguchi, "Influences of target surface small-scale rectangle roughness on impingement jet array heat transfer," *Int. J. Heat Mass Transf.*, vol. 110, pp. 805–816, 2017. https://doi.org/10.1016/j.ijheatmasstransfer.2017.03.061

[13] P. Xu, A. Sasmito, S. Qiu, A. Mujumdar, L. Xu, and L. Geng, "Heat transfer and entropy generation in air jet impingement on a model rough surface," *Int. Commun. Heat Mass Transf.*, vol. 72, pp. 48–56, 2016. https://doi.org/10.1016/j.icheatmasstransfer.2016.01.007

[14] R. K. Ajeel, W. S. I. W. Salim, and K. Hasnan, "Experimental and numerical investigations of convection heat transfer in corrugated channels using alumina nanofluid under a turbulent flow regime," *Chem. Eng. Res. Des.*, vol. 148, pp. 202–217, 2019. https://doi.org/10.1016/j.cherd.2019.06.003

[15] L. C. Yang, Y. Asako, Y. Yamaguchi, and M. Faghri, "Numerical prediction of transitional characteristics of flow and heat transfer in a corrugated duct," *J. Heat Transfer.*, vol. 119, no. 1, pp. 62–69, 1997. https://doi.org/10.1115/1.2824101

[16] J. Blazek, *Computational Fluid Dynamics: Principles and Applications*. ELSEVIER, 2015.

[17] C. J. Chen, *Fundamentals of Turbulence Modelling*. CRC Press, 1997.

[18] L. Zhang and D. Che, "Influence of corrugation profile on the thermalhydraulic performance of cross-corrugated plates," *Numer. Heat Transf. Part A Appl.*, vol. 59, no. 4, pp. 267–296, 2011. https://doi.org/10.1080/10407782.2011.540963

[19] M. Kalteh, A. Abbassi, M. Saffar-Avval, and J. Harting, "Eulerian–eulerian two-phase numerical simulation of nanofluid laminar forced convection in a microchannel," *Int. J. Heat Fluid Flow*, vol. 32, no. 1, pp. 107–116, 2011. https://doi.org/10.1016/j.ijheatfluidflow.2010.08.001

[20] O. Manca, S. Nardini, and D. Ricci, "A numerical study of nanofluid forced convection in ribbed channels," *Appl. Therm. Eng.*, vol. 37, pp. 280–292, 2012. https://doi.org/10.1016/j.applthermaleng.2011.11.030

[21] K. Esmailpour, B. Bozorgmehr, S. M. Hosseinalipour, and A. S. Mujumdar, "Entropy generation and second law analysis of pulsed impinging jet," *Int. J. Numer. Methods Heat Fluid Flow*, vol. 25, no. 5, pp. 1089–1106, 2015. https://doi.org/10.1108/HFF-05-2014-0148

[22] H. K. Versteeg and W. Malalasekera, *An Introduction to Computational Fluid Dynamics: The Finite Volume Method*. Pearson Education, 2007.

[23] L. Mangani and C. Bianchini, "Heat transfer applications in turbomachinery," in *Proceedings of the OpenFOAM International Conference*, 2007.

[24] B. Buonomo, O. Manca, N. S. Bondareva, and M. A. Sheremet, "Thermal and fluid dynamic behaviors of confined slot jets impinging on an isothermal moving surface with nanofluids," *Energies*, vol. 12, no. 11, 2019. https://doi.org/10.3390/en12112074

Nomenclature

Symbol	Description	Units
A	Rib height	mm
B	Rib location	mm
D	Rib length	mm
$C_1, C_2, C\mu$	Empirical constant for turbulence model	——
C_p	Specific heat capacity	$(\mathrm{J/kg\,K})$
f	Friction factor	——
f_1, f_2, f_μ	Damping function	——
H	Channel height	mm
k	Turbulent kinetic energy	$\mathrm{m\,s^{-2}}$
k_f	Thermal conductivity of base fluid	$W\ \mathrm{m^{-1}}K^{-1}$
L	Target surface length	mm
Nu	Nusselt number	——
p	Pressure drop	pa
Pr	Prandtl number	——
Pr_t	Turbulent Prandtl number	——
q_p	Heat flux	$W\ \mathrm{m^{-2}}$
Re	Reynolds number $Re = \rho v_{in}/\mu$	——
T	Temperature	K
Z	Slot jet width	mm
S	Entropy generation	$W\ \mathrm{m^{-3}}K^{-1}$
u, v	Velocities components	$\mathrm{m\,s^{-1}}$
x, y	2D Cartesian coordinates	mm

Greek symbols

μ	Dynamic viscosity	$\mathrm{N\,s\,m^{-2}}$
μ_t	Turbulent dynamic viscosity	$\mathrm{N\,s\,m^{-2}}$
ρ	Density	$\mathrm{kg\,m^{-3}}$
ε	Dissipation rate of turbulent kinetic energy	$\mathrm{m^2\ s^{-3}}$
$\sigma_{\boldsymbol{k}}, \boldsymbol{\sigma_\varepsilon}$	Empirical constant for turbulence model	——
Δp	Pressure drop	pa
Γ	Diffusion coefficient	——
ξ, η	Body-fitted coordinates	——

Subscripts

b	Bulk fluid	——
eff	Effective	——
f	Fluid	——
in	Inlet	——-
p	Plate	——
r	Rib	——
s	Smooth target	——
th	Thermal	——
vi	Viscous	——
–	Average	——-

Abbreviations

FVM	Finite Volume Method	——
PEC	Performance Evaluation Criteria	—-